ELSEVIER

Thin-Walled Structures 40 (2002) 595–609

THIN-WALLED STRUCTURES

www.elsevier.com/locate/tws

Contact based delamination and fracture analysis of composites

S. Mohammadi *, S. Forouzan-sepehr, A. Asadollahi

Department of Civil Engineering, University of Tehran, Tehran, Iran

Received 10 July 2001; received in revised form 12 November 2001; accepted 20 November 2001

Abstract

A new approach based on the concepts of the discrete element method, is presented for impact resistance analysis of composites. The method is capable of analysing the progressive fracturing and fragmentation behaviour, as well as potential post-cracking interactions caused by the newly created crack sides and segments. The imminence of a material crack is monitored by an anisotropic Hoffman model. To avoid the mesh dependency of the results, a bilinear local softening model, based on modes I and II, is also adopted in this study to account for release of energy and redistribution of forces that caused the formation of a crack. A special re-meshing method has been developed to geometrically model an individual crack by splitting the element, separating the failed node, creating new nodes and dividing the neighbouring elements to preserve the compatibility conditions. Numerical simulations have been performed to assess the performance of the proposed algorithm. The method has proved to be an efficient approach for impact analysis of composites undergoing progressive delamination and cracking.

Keywords: Impact; Cracking; Composites; Delamination; Discrete element method

1. Introduction

The phenomenon of failure by catastrophic crack propagation poses problems in all engineering applications. Therefore, development of reliable models for determin-

* Corresponding author.
E-mail address: smoham@shafagh.ut.ac.ir (S. Mohammadi).

0263-8231/02/$ - see front matter © 2002 Published by Elsevier Science Ltd.
PII: S0263-8231(02)00014-9

ing the failure behaviour of advanced materials, such as composites, is vitally important.

Nowadays composite materials are widely used in manufacturing aircraft, helicopters, cars and satellite systems, because of their lightness, high strength-to-weight ratio, good damping characteristics, and high fatigue strength.

One of the major problems in designing composite structures is their vulnerability to transverse impact, which can cause significant internal damage in terms of delamination, matrix cracking and fragmentation. Because of the important role of the problem in the reduction of load bearing capacity and performance of a structure, numerous experimental and analytical investigations have been performed so far. In early simulations, continuum elasticity was frequently used to formulate the governing equations [11–13]. The main disadvantage of these schemes was their restriction to linear geometry of laminates [10]. Afterwards, more realistic models were achieved through the development of contact-interaction algorithms [1,5,6,16].

Introducing interface elements based on fracture mechanics, numerical simulation of crack initiation and propagation by finite elements has become more rational and popular in recent studies [2,15]. Nevertheless, the finite element techniques, which are rooted in the concepts of continuum mechanics, are not suited to general fracture propagation and fragmentation problems. In contrast, the discrete element method (DEM) is specifically designed to solve problems that exhibit strong discontinuities in material and geometric behaviour.

The DEM idealises the whole medium into an assemblage of individual bodies, which in addition to their own deformable response, interact with each other (through a contact type interaction) to capture the characteristics of the discontinuum and to give the same response as the medium itself. It is, therefore, a finite element modelling coupled with the concepts of contact mechanics.

In this paper, some of the main aspects of crack initiation/propagation procedures by DEM in typical problems of impact on composites are discussed. Consideration of some benchmark and practical problems will help in verifying the performance of the proposed algorithm.

2. Combined FE/DE modelling of composites

The aim of this study is to develop a reliable numerical method for assessing impact-induced damage in composites, based on the principles of plasticity, contact mechanics and fracture mechanics. A contact-based methodology is employed for modelling and controlling of plies bonding/debonding. The interlaminar behaviour in the post-delamination phase, such as slipping and crack-face interactions, are also considered. Employing an algorithm based on 3D contact mechanics in failure analysis of composites is a novel technique, and a more accurate and reliable analysis of this complex behaviour is obtained. In addition to 3D contact models, a 3D anisotropic bonding model with strain softening behaviour has also been developed and implemented to investigate interlaminar crack propagation (delamination).

In this study, modelling of composite shells subjected to impact loading is perfor-

med by the use of the finite/DEM. The potentially susceptible damage region is modelled using a discrete element mesh, and the rest of the specimen is modelled with coarser solid elements to reduce the analysis time (Fig. 1(a)). Each discrete element is discretised by a finite element mesh of equal or different size; a finer mesh is used for the plies closer to the impact region, and a coarser mesh for the furthest ones. The interlaminar characteristics of plies such as debonding, impenetrability, friction and sliding determine connection (bonding) states of the adjacent discrete elements (Fig. 1(b)). The discrete element system and the finite element mesh are connected together by transition interfaces, which are defined as normal interfaces with very high bonding strengths, preventing debonding under all stress conditions. Non-linear material properties (using the Hoffman anisotropic yield criterion) and geometric non-linearities (large deformation) are also considered in the FE formulation [9].

3. Boundary value problem

The dynamic boundary value formulation for a system consisting of the body Ω with the boundary Γ can be expressed as

$$\mathscr{W}^{\text{inertia}} + \mathscr{W}^{\text{int}} = \mathscr{W}^{\text{ext}} + \mathscr{W}^{\text{con}} \tag{1}$$

where the terms denote the virtual work of inertial forces, internal forces, external forces and contact forces respectively

$$\mathscr{W}^{\text{inertia}} = \int_{\Omega} \delta \mathbf{u}^{\mathrm{T}} \boldsymbol{\rho} \ddot{\mathbf{u}} \mathrm{d}\Omega \tag{2}$$

$$\mathscr{W}^{\text{int}} = \int_{\Omega} \delta \boldsymbol{\varepsilon}^{\mathrm{T}} \boldsymbol{\sigma} \mathrm{d}\Omega \tag{3}$$

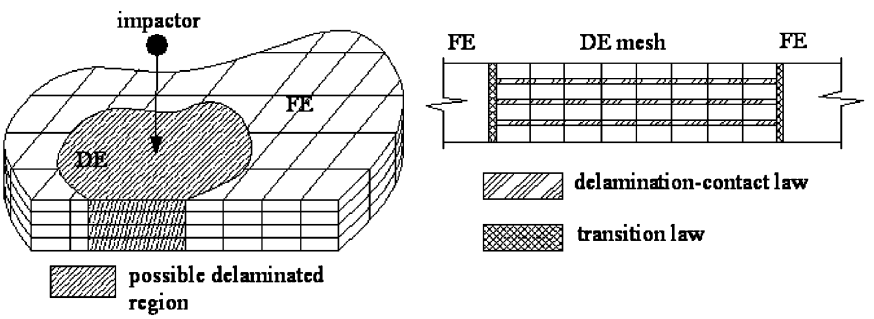

Fig. 1. Composite specimen subjected to impact loading: (a) discrete/finite element mesh; (b) interfacial regions.

$$\mathscr{W}^{\text{ext}} = \int_{\Omega} \delta\mathbf{u}^{\mathrm{T}}\mathbf{b}\mathrm{d}\Omega + \int_{\Gamma_{\text{trac}}} \delta\mathbf{u}^{\mathrm{T}}\mathbf{t}\mathrm{d}\Gamma + \int_{\Gamma_{\text{fix}}} \delta\mathbf{u}^{\mathrm{T}}\mathbf{r}\mathrm{d}\Gamma \tag{4}$$

$$\mathscr{W}^{\text{con}} = \int_{\Gamma_{\text{con}}} \delta\mathbf{g}^{\mathrm{T}}\boldsymbol{\sigma}^{\mathrm{c}}\mathrm{d}\Gamma \tag{5}$$

in which Γ_{trac}, Γ_{con} and Γ_{fix} are the regions of traction forces, contact and fixity, respectively; $\boldsymbol{\rho}$ is the matrix of mass density; $\mathbf{b}$, $\mathbf{t}$ and $\mathbf{r}$ are the vectors of body forces, traction forces and reactions, respectively; $\boldsymbol{\sigma}$ is the Cauchy stress tensor, $\boldsymbol{\varepsilon}$ is its conjugate strain tensor, $\mathbf{u}$ is the displacement vector and $\boldsymbol{\sigma}^{\mathrm{c}}$ is the contact stress vector; finally, $\mathbf{g}$ denotes the contact gap vector. Eq. (1) can be rewritten in matrix form as

$$\mathbf{M}\ddot{\mathbf{u}} + \mathbf{f}^{\text{int}} = \mathbf{f}^{\text{ext}} + \mathbf{f}^{\text{con}} \tag{6}$$

where $\mathbf{M}$ denotes the mass matrix, and $\mathbf{f}^{\text{int}}$, $\mathbf{f}^{\text{ext}}$, $\mathbf{f}^{\text{con}}$ denote the internal, external and contact-force vectors, respectively.

The explicit central-difference method, which is a popular fast method frequently used for general large-scale impact problems, is adopted as the time integration technique [10].

4. Contact constitutive relationship

A bilinear strain-softening model [7,8], together with the penalty method to impose impenetrability and frictional contact, are employed in bonding interfaces. A contact gap vector can be described as

$$\mathbf{g} = [g_{\mathrm{N}}, \mathbf{g}_{\mathrm{T}}]^{\mathrm{T}} \tag{7}$$

where g_{N} is the normal distance between contact node S and contact segment M_1M_2 in 2D, or $M_1M_2M_3M_4$ in 3D. The parameter $\mathbf{g}_{\mathrm{T}}$ is a tangential vector whose size is equal to the distance between the projection of the contact node in the current configuration C^{t0} and the initial configuration S^0 (Fig. 2). The components of the gap vector determine the state of two adjacent plies as shown in Table 1.

Thus, combining the bilinear strain-softening model with the penalty method leads to constitutive interfacial relationships in pure modes I and II (Fig. 3), where g_{T} is the magnitude of vector $\mathbf{g}_{\mathrm{T}}$, $\bar{\sigma}_{\mathrm{N}}$ and $\bar{\sigma}_{\mathrm{T}}$ are the threshold tensile and shear strength of the binder between plies, while $\bar{g}_0^{\mathrm{N}}$ and $\bar{g}_0^{\mathrm{T}}$ are the related displacements. The parameters $\bar{g}_{\max}^{\mathrm{N}}$ and $\bar{g}_{\max}^{\mathrm{T}}$ are the maximum normal and tangential displacements, which the binder can bear without debonding. Fracture energy release rate for modes I and II are defined as the area under the normal and tangential stress–displacement curves, respectively;

$$G_{\mathrm{cI}} = 1/2\bar{\sigma}_{\mathrm{N}}\bar{g}_{\max}^{\mathrm{N}} \tag{8}$$

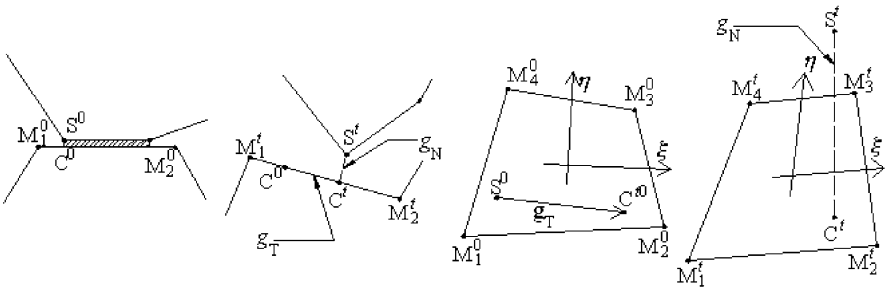

Fig. 2. Normal and tangential gaps in 2D and 3D problems: (a) initial configuration (bounded plies) in 2D; (b) current configuration in 2D; (c) initial configuration (bounded plies) in 3D; (d) current configuration in 3D.

Table 1
Plies states in relation to gap conditions

Fracture mode	Gap condition	Plies state
Pure mode I	$g_N < 0$	Penetration
	$0 < g_N < \bar{g}^N_{max}$	Opening without debonding
	$g_N > \bar{g}^N_{max}$	Opening of debonded plies
Pure mode II	$g_T = \|\mathbf{g}_T\| < \bar{g}^T_{max}$	Shearing without cracking
	$g_T = \|\mathbf{g}_T\| > \bar{g}^T_{max}$	Friction and sliding of two debonded plies

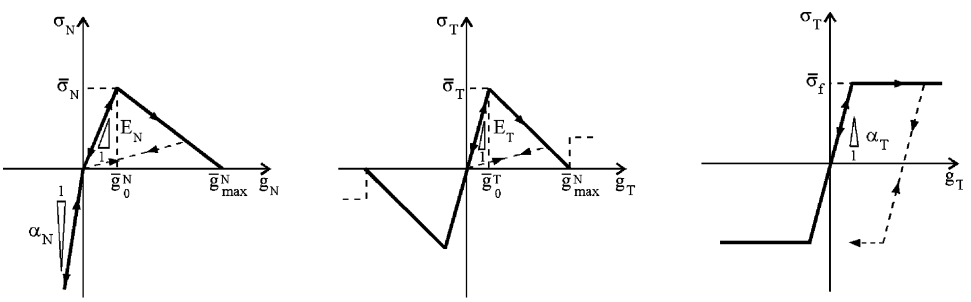

Fig. 3. Normal and tangential contact stress-gap vector magnitude diagram: (a) pure normal mode; (b) pure tangential mode in adhesion phase; (c) pure tangential mode in friction phase.

$$G_{cII} = 1/2\bar{\sigma}_T\bar{g}^T_{max} \tag{9}$$

Thus, $\bar{g}^N_{max}$ and $\bar{g}^T_{max}$ are known since G_{cI} and G_{cII} are assumed to be constant material properties, while $\bar{\sigma}_N$ and $\bar{\sigma}_T$ can be obtained by experiments; α_N and α_T are the penalty parameters, and $\bar{\sigma}_f$ is the maximum friction stress between plies:

$$\bar{\sigma}_f = \mu\langle-\sigma_N\rangle \tag{10}$$

where μ is the Coulomb coefficient of dry friction and $\langle\cdot\rangle$ denotes the Macaulay function, that is

$$\langle x-a\rangle = \begin{cases} x-a & ;x\geq a \\ 0 & ;x < a \end{cases} \tag{11}$$

Fig. 3 shows the stress–displacement relationships for pure modes I and II. In practice, however, initiation of delamination in any mode will affect the other modes of fracture. Here, a coupled delamination damage model introduced in Mi et al. [8] has been employed to include these effects. The model is based on the extent of damage, defined by:

$$\kappa = \sqrt{\left\langle \frac{g_{\mathrm{N}}}{\bar{g}_0^{\mathrm{N}}} \right\rangle^2 + \left(\frac{g_{\mathrm{T}}}{\bar{g}_0^{\mathrm{T}}} \right)^2} - 1 \tag{12}$$

in which the use of the Macaulay function for the normal displacement is due to the fact that only tensile displacement (opening) affects delamination. According to this model, delamination will initiate as soon as κ exceeds zero. Combination of this model and the Penalty method leads to the constitutive relationship between interfacial stresses and their related displacements, that is

$$\boldsymbol{\sigma}^{\mathrm{c}} = [\sigma_{\mathrm{N}}\boldsymbol{\sigma}_{\mathrm{T}}]^{\mathrm{T}} = \mathbf{D}^{\mathrm{c}}\mathbf{g}, \tag{13}$$

$$\mathbf{D}^{\mathrm{c}} = \mathrm{Diag}[D_{\mathrm{N}}{}^{\mathrm{c}}(\mathbf{g}), D_{\mathrm{T}}{}^{\mathrm{c}}(\mathbf{g}), D_{\mathrm{T}}{}^{\mathrm{c}}(\mathbf{g})] \tag{14}$$

Defining three parameters $S_{\mathrm{N}}(\kappa)$, $S_{\mathrm{T}}(\kappa)$ and g^*_{Tu} as

$$S_{\mathrm{N}}(\kappa) = \frac{\kappa}{1+\kappa} \cdot \frac{\bar{g}^{\mathrm{N}}_{\max}}{\bar{g}^{\mathrm{N}}_{\max} - \bar{g}_0^{\mathrm{N}}} \tag{15}$$

$$S_{\mathrm{T}}(\kappa) = \frac{\kappa}{1+\kappa} \cdot \frac{\bar{g}^{\mathrm{T}}_{\max}}{\bar{g}^{\mathrm{T}}_{\max} - \bar{g}_0^{\mathrm{T}}} \tag{16}$$

$$g^*_{\mathrm{Tu}} = \bar{g}_0^{\mathrm{T}} \sqrt{\left\langle \left(\frac{\bar{g}^{\mathrm{T}}_{\max}}{\bar{g}_0^{\mathrm{T}}} \right)^2 - \left\langle \frac{g_{\mathrm{N}}}{\bar{g}_0^{\mathrm{N}}} \right\rangle^2 \right\rangle} \tag{17}$$

results in

$$D^{\mathrm{c}}_{\mathrm{N}}(\mathbf{g}) = \begin{cases} \alpha_{\mathrm{N}} & ;g_{\mathrm{N}} \leq 0 \\ E_{\mathrm{N}} & ;g_{\mathrm{N}} > 0,\ \kappa \leq 0 \\ (1-S_{\mathrm{N}}(\kappa))E_{\mathrm{N}} & ;g_{\mathrm{N}} > 0,\ S_{\mathrm{N}}(\kappa) < 1 \\ 0 & ;g_{\mathrm{N}} > 0,\ S_{\mathrm{N}}(\kappa) \geq 1 \end{cases} \tag{18}$$

$$D_{\mathrm{T}}^{\mathrm{c}}(\mathbf{g}) = \begin{cases} E_{\mathrm{T}} & ;\kappa \le 0 \\ (1-S_{\mathrm{T}}(\kappa))E_{\mathrm{T}} & ;\kappa > 0, S_{\mathrm{T}}(\kappa) < 1 \\ \left(\dfrac{g_{\mathrm{Tu}}{}^{*}}{g_{\mathrm{T}}} - 1\right)\alpha_{\mathrm{T}} & ;S_{\mathrm{T}}(\kappa) \ge 1, g_{\mathrm{T}} < g_{\mathrm{Tu}}{}^{*} + \dfrac{\bar{\sigma}_{\mathrm{f}}}{\alpha_{\mathrm{T}}} \\ \dfrac{\bar{\sigma}_{\mathrm{f}}}{g_{\mathrm{T}}} & ;S_{\mathrm{T}}(\kappa) \ge 1, g_{\mathrm{T}} \ge g_{\mathrm{Tu}}{}^{*} + \dfrac{\bar{\sigma}_{\mathrm{f}}}{\alpha_{\mathrm{T}}} \end{cases} \tag{19}$$

5. Hoffman anisotropic material model

According to the Hoffman criterion [4], which can be assumed to be a generalisation of the Hill criterion [3] with different tensile and compressive yield strengths, the failure surface is described by a quadratic function of nine independent variables: three tensile yield strengths $\bar{\sigma}_{ii\mathrm{T}}$, three compressive yield strengths $\bar{\sigma}_{ii\mathrm{C}}$ and three shear yield strengths $\bar{\sigma}_{ij\mathrm{S}}(i \neq j)$. It may be defined as

$$\Phi = 1/2\boldsymbol{\sigma}^{\mathrm{T}}\mathbf{P}_{\alpha}\boldsymbol{\sigma} + \boldsymbol{\sigma}^{\mathrm{T}}\mathbf{p}_{\alpha} - \bar{\sigma}^{2} = 0 \tag{20}$$

in which

$$\boldsymbol{\sigma} = [\sigma_{11}\ \sigma_{22}\ \sigma_{33}\ \sigma_{12}\ \sigma_{13}\ \sigma_{23}]^{\mathrm{T}} \tag{21}$$

$$\mathbf{P}_{\alpha} = \begin{bmatrix} 2(\alpha_{12}+\alpha_{13}) & -2\alpha_{12} & -2\alpha_{13} & 0 & 0 & 0 \\ -2\alpha_{12} & 2(\alpha_{12}+\alpha_{23}) & -2\alpha_{23} & 0 & 0 & 0 \\ -2\alpha_{13} & -2\alpha_{23} & 2(\alpha_{13}+\alpha_{23}) & 0 & 0 & 0 \\ 0 & 0 & 0 & 6\alpha_{44} & 0 & 0 \\ 0 & 0 & 0 & 0 & 6\alpha_{55} & 0 \\ 0 & 0 & 0 & 0 & 0 & 6\alpha_{66} \end{bmatrix} \tag{22}$$

$$\mathbf{p}_{\alpha} = [\alpha_{11}\ \alpha_{22}\ \alpha_{33}\ 0\ 0\ 0]^{\mathrm{T}} \tag{23}$$

The material properties α_{ij} are given by

$$\begin{aligned} &\alpha_{11} = \bar{\sigma}^{2}\left(\frac{\bar{\sigma}_{11\mathrm{C}} - \bar{\sigma}_{11\mathrm{T}}}{\bar{\sigma}_{11\mathrm{C}}\bar{\sigma}_{11\mathrm{T}}}\right),\ \alpha_{22} = \bar{\sigma}^{2}\left(\frac{\bar{\sigma}_{22\mathrm{C}} - \bar{\sigma}_{22\mathrm{T}}}{\bar{\sigma}_{22\mathrm{C}}\bar{\sigma}_{22\mathrm{T}}}\right),\ \alpha_{33} = \bar{\sigma}^{2}\left(\frac{\bar{\sigma}_{33\mathrm{C}} - \bar{\sigma}_{33\mathrm{T}}}{\bar{\sigma}_{33\mathrm{C}}\bar{\sigma}_{33\mathrm{T}}}\right) \\ &\alpha_{44} = \frac{\bar{\sigma}^{2}}{3\bar{\sigma}_{12}{}^{2}},\ \alpha_{55} = \frac{\bar{\sigma}^{2}}{3\bar{\sigma}_{13}{}^{2}},\ \alpha_{66} = \frac{\bar{\sigma}^{2}}{3\bar{\sigma}_{23}{}^{2}} \\ &\alpha_{12} = \frac{\bar{\sigma}^{2}}{2}\left(\frac{1}{\bar{\sigma}_{11\mathrm{T}}\bar{\sigma}_{11\mathrm{C}}} + \frac{1}{\bar{\sigma}_{22\mathrm{T}}\bar{\sigma}_{22\mathrm{C}}} - \frac{1}{\bar{\sigma}_{33\mathrm{T}}\bar{\sigma}_{33\mathrm{C}}}\right) \\ &\alpha_{13} = \frac{\bar{\sigma}^{2}}{2}\left(\frac{1}{\bar{\sigma}_{11\mathrm{T}}\bar{\sigma}_{11\mathrm{C}}} + \frac{1}{\bar{\sigma}_{33\mathrm{T}}\bar{\sigma}_{33\mathrm{C}}} - \frac{1}{\bar{\sigma}_{22\mathrm{T}}\bar{\sigma}_{22\mathrm{C}}}\right) \\ &\alpha_{23} = \frac{\bar{\sigma}^{2}}{2}\left(\frac{1}{\bar{\sigma}_{22\mathrm{T}}\bar{\sigma}_{22\mathrm{C}}} + \frac{1}{\bar{\sigma}_{33\mathrm{T}}\bar{\sigma}_{33\mathrm{C}}} - \frac{1}{\bar{\sigma}_{11\mathrm{T}}\bar{\sigma}_{11\mathrm{C}}}\right) \end{aligned} \tag{24}$$

For integration of the flow rule in a finite time step, the backward Euler method, coupled with the Newton–Raphson iterative scheme, is used [14]. For the *j*th iteration of the *i*th load step, the total strain is assumed to consist of an elastic and plastic part

$$\mathbf{\Delta\varepsilon}_j = \mathbf{\Delta\varepsilon}_j^{\mathrm{el}} + \mathbf{\Delta\varepsilon}_j^{\mathrm{pl}} \tag{25}$$

where

$$\mathbf{\Delta\varepsilon}_j^{\mathrm{el}} = \mathbf{D}^{-1}\boldsymbol{\sigma}_j,\ \mathbf{\Delta\varepsilon}_j^{\mathrm{pl}} = \Delta\lambda_j\frac{\partial\Phi}{\partial\boldsymbol{\sigma}_j} \tag{26}$$

Then, the final stress at the end of the iteration can be obtained from

$$\boldsymbol{\sigma}_j = \mathbf{D}(\mathbf{I} + \Delta\lambda_j\mathbf{D}\mathbf{P}_\alpha)^{-1}(\boldsymbol{\varepsilon}_{i-1}^{\mathrm{el}} + \mathbf{\Delta\varepsilon}_j - \Delta\lambda_j\mathbf{p}_\alpha) \tag{27}$$

with $\Delta\lambda_j$ obtainable results from the following iterative equation

$$\Delta\lambda_j^{k+1} = \Delta\lambda_j^{k} - \left.\frac{\Phi(\Delta\lambda_j)}{\dfrac{\partial\Phi}{\partial\Delta\lambda_j}}\right|_{\Delta\lambda_j^{k+1}} \tag{28}$$

where

$$\frac{\partial\Phi(\Delta\lambda)}{\partial\Delta\lambda_j} = -(\mathbf{P}_\alpha\boldsymbol{\sigma}_j + \mathbf{p}_\alpha)^{\mathrm{T}}(\mathbf{D}^{-1} + \Delta\lambda_j\mathbf{P}_\alpha)^{-1}(\mathbf{P}_\alpha\boldsymbol{\sigma}_j + \mathbf{p}_\alpha) \tag{29}$$

For further details, see Ref. [14].

6. Numerical studies

6.1. Fracture and delamination buckling analysis of an orthotropic composite beam

Two orthotropic composite specimens with different laminate layouts are considered. Each laminate is composed of T300/976 graphite epoxy prepreg tape (Table 2 [6]). The composite $[90_n,\ 0_n,\ 90_n]$ and $[0_n,\ 90_{2n},\ 0_n]$ ply layouts are assigned to the beams with (LHW = 10.16,0.249,2.54cm) and (LHW = 7.62,0.228,2.63cm)

Table 2
Material properties of the orthotropic composite beam

Ply longitudinal modules: $E_{xx} = 139.3 \times 10^3$MPa	Ply transverse modules: $E_{yy} = 9.7 \times 10^3$MPa
Poisson's ration: $\nu = 0.3$	Density: $\rho = 1380-2000\mathrm{kg/m^3}$
Ply longitudinal tensile strength: $X_{\mathrm{t}} = 1150$MPa	Ply transverse compressive strength: $X_{\mathrm{c}} = 1120$MPa
Ply transverse tensile strength: $Y_{\mathrm{t}} = 40$MPa	Ply transverse compressive strength: $Y_{\mathrm{c}} = 170$MPa
Ply shear strength: $S = 100$MPa	

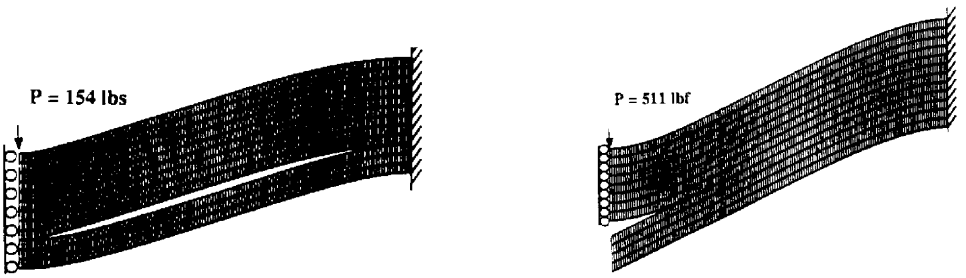

Fig. 4. Results reported in Ref. [6]: (a) $[90_n,\ 0_n,\ 90_n]$; (b) $[0_n,\ 90_{2n},\ 0_n]$.

geometric descriptions, respectively. The specimens are subjected to quasi-static concentrated loading $P = 2300$kN applied at their centre lines. Eight and nine layer finite/discrete element meshes were used to model half of the beams, respectively. The results in Reference [6] are shown in fig. 4.

Figs. 5(a) and (b) illustrate the deformed modes of delaminated layers for both beams. Liu et al [6] reported the same patterns at the interface of the bottom $[0_n]$ and $[90_n]$ plies for the $[0_n,\ 90_{2n},\ 0_n]$ specimen. However, no buckling mode was reported for the $[90_n,\ 0_n,\ 90_n]$ specimen (Fig. 4(a)).

In addition to a delamination analysis, a fracture analysis was performed to predict the real damage modes of the beams (Fig. 5(c) and (d)). Matrix cracking across the

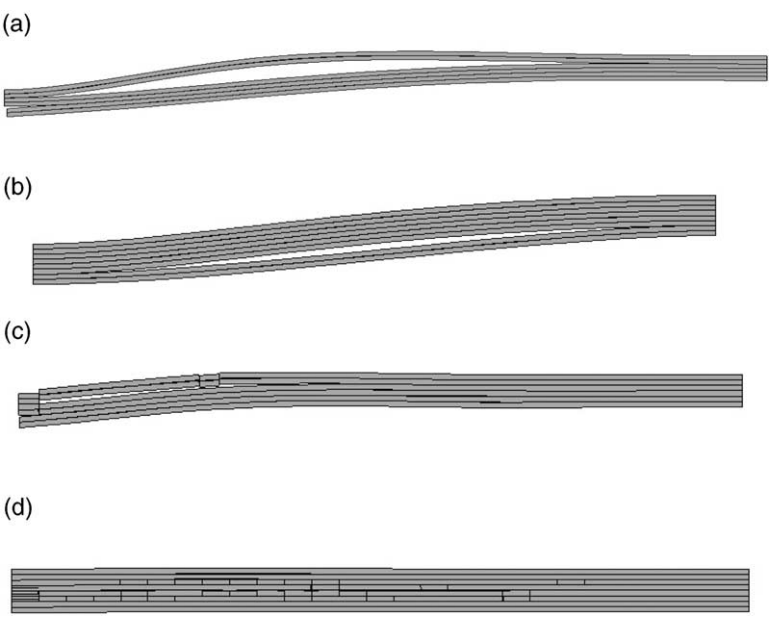

Fig. 5. Results obtained by combined FE/DE analysis: (a), (b) delamination analysis; (c), (d) delamination and fracture analysis.

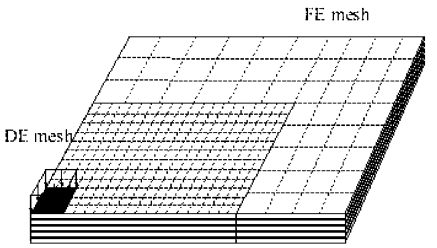

Model size = $0.0762 \times 0.0508 \times 0.00444$ m

Ply region = $[90_n, 0_n, 90_n, 0_n, 90_n]$

DE region = 0.050×0.035 m

$E_{xx} = 152.4\text{E}3$ MPa	$E_{yy} = 10.7\text{E}3$ MPa
$\nu = 0.35$	$\rho = 1.55\text{E}3\,\text{kg/m}^3$
$X_t = 2772$ MPa	$X_c = 3100$ MPa
$Y_t = 79.3$ MPa	$Y_c = 231.0$ MPa
$S = 132.8$ MPa	

Fig. 6. FE/DE mesh of one quarter of the composite specimen.

thickness of the top layer of the first specimen prevents the formation of a buckling mode, and the overall behaviour of the specimen reduces nearly to that of an unbonded multi-layer beam. The fracture patterns for the second specimen are mainly concentrated within the weak mid layer of the beam, especially around the loading region, while extensive delaminations are formed at the interfaces of $[90_n]$ and $[0_n]$ layers.

6.2. Rectangular plate-delamination analysis

A composite plate specimen subjected to a triangular load applied from 0 to 5 μs with a peak force of 5 kN is investigated. This modelling is a numerical simulation of the experiments undertaken in Worswick et al. [17]. Because of symmetry, only one quarter of the plate is modelled (Fig. 6). Also, only the central region of this model is meshed by discrete elements. To ensure the mesh independency of the results, the analysis is performed with both a coarse and a finer mesh. The deformed shape of the plate at $t = 0.00018$s is illustrated in Fig. 7(a). Fig. 7(b) depicts a comparison of the displacement history of the centre of the plate (both top and

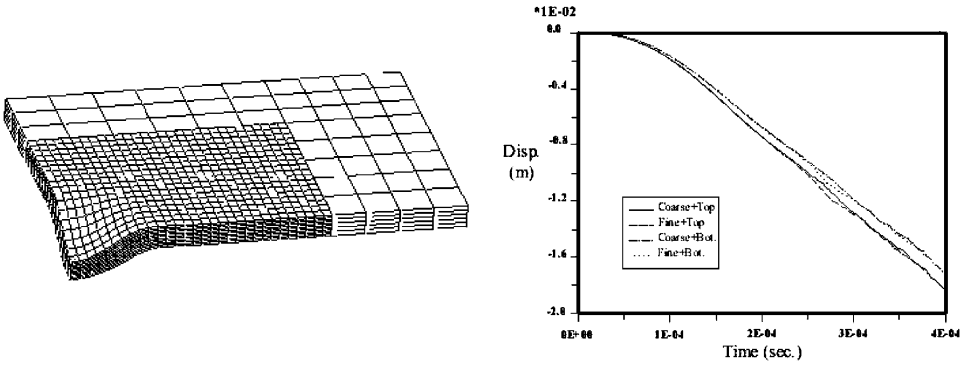

Fig. 7. (a) Deformed shape of the plate at $t = 0.00018$s. (b) Displacement history of the central point.

bottom points across the thickness) for both coarse and fine meshes. Also, Fig. 8 compares the delamination patterns of the top and bottom plies interfaces of the fine mesh at different time steps.

It should be noted that these results were achieved without considering a material fracture analysis and only delamination was activated. In practice, however, the illustrated large deformations will certainly involve extensive material fracture and failure.

6.3. Square plate-delamination and fracture analysis

A composite specimen (Fig. 9) subjected to a similar loading condition as in th previous example test is considered. This modelling is also a numerical simulation of the experiments undertaken in Worswick et al. [17]. The fracture patterns of the plate at $t = 0.0136$s and $t = 0.0245$s are illustrated in Fig. 10(a) and (b). The shaded areas represent the fractured region at different layers for the fine mesh analysis. Also, Fig. 11 illustrates the delamination patterns of the top to bottom plies interfaces of the fine mesh at times $t = 0.0136$s and $t = 0.0245$s.

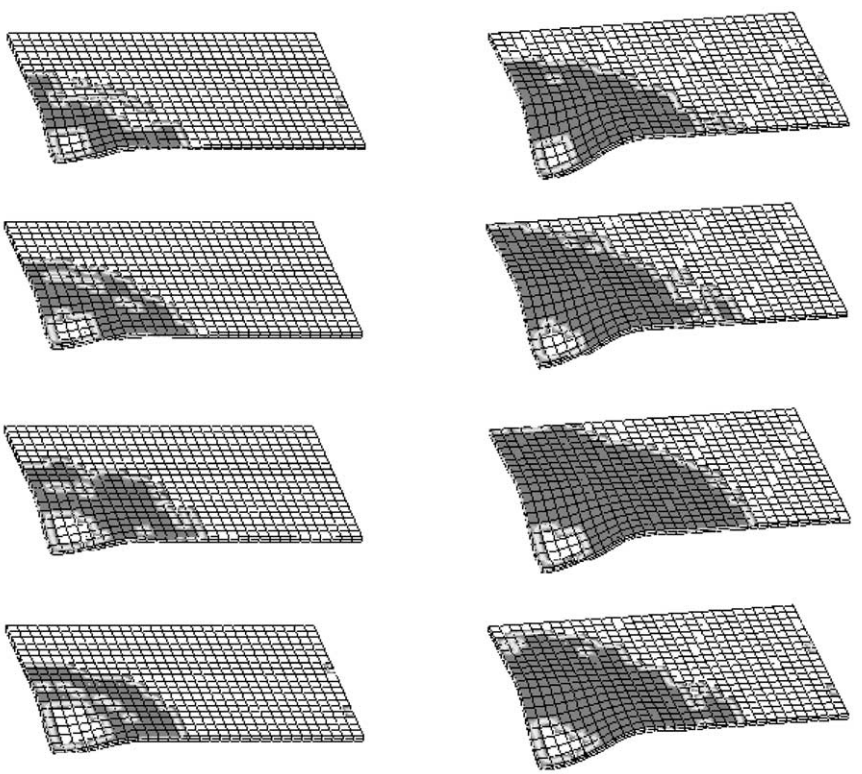

Fig. 8. Delamination patterns at the top to bottom interfaces of the composite mesh: at (a) $t =$ 0.00012s and (b) $t = 0.00018$s.

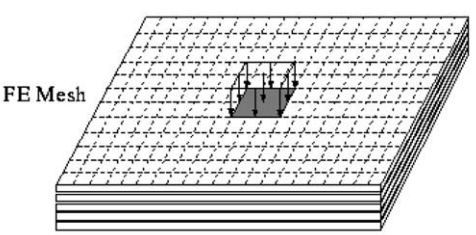

Model size = $0.1524 \times 0.1524 \times 0.00444$ m

Ply region = $[+45_n, -45_n, +45_n, -45_n, +45_n]$

$E_{xx} = 152.4\text{E}3$ MPa	$E_{yy} = 10.7\text{E}3$ MPa
$\nu = 0.35$	$\rho = 0.35\,\text{kg/m}^3$
$X_t = 2772$ MPa	$X_c = 3100$ MPa
$Y_t = 79.3$ MPa	$Y_c = 231.0$ MPa
$S = 132.8$ MPa	

Fig. 9. FE/DE mesh of the composite specimen.

More than 30,000 unstructured pentahedral elements and 25,000 nodes were initially used for modelling the composite plate. Because of geometric modelling of cracks and re-meshing procedures, the final model consisted of more than 38,000 elements and 40,000 nodes. The changing (increasing) nature of the size of model requires a rather sophisticated data base structure and programming techniques to be incorporated in the combined finite/discrete element code.

7. Conclusions

A contact based method has been successfully developed for 3D damage analysis of composites. The initiation and propagation of cracks have been considered by using a bilinear strain-softening model, which has been found to be adequately accurate. The penalty method has been employed to impose impenetrability and post-debonding behaviours of plies as well as post-cracking of individual layers. Several numerical tests have been used to assess the performance of the method, showing the power of the algorithm for numerical simulation of impact loading on composite structures. The method is expected to perform well for other similar applications such as masonry structures which exhibit progressive fracturing due to dynamic and moving load conditions.

Acknowledgements

The first author would like to gratefully acknowledge Prof. D.R.J. Owen and Prof. D. Perić of the University of Wales, Swansea for their contribution in the developing stage of this work. The authors would like to acknowledge the support received from the ‘University of Tehran, Vice Chancellor for Research’ under the grant number 614/2/627.

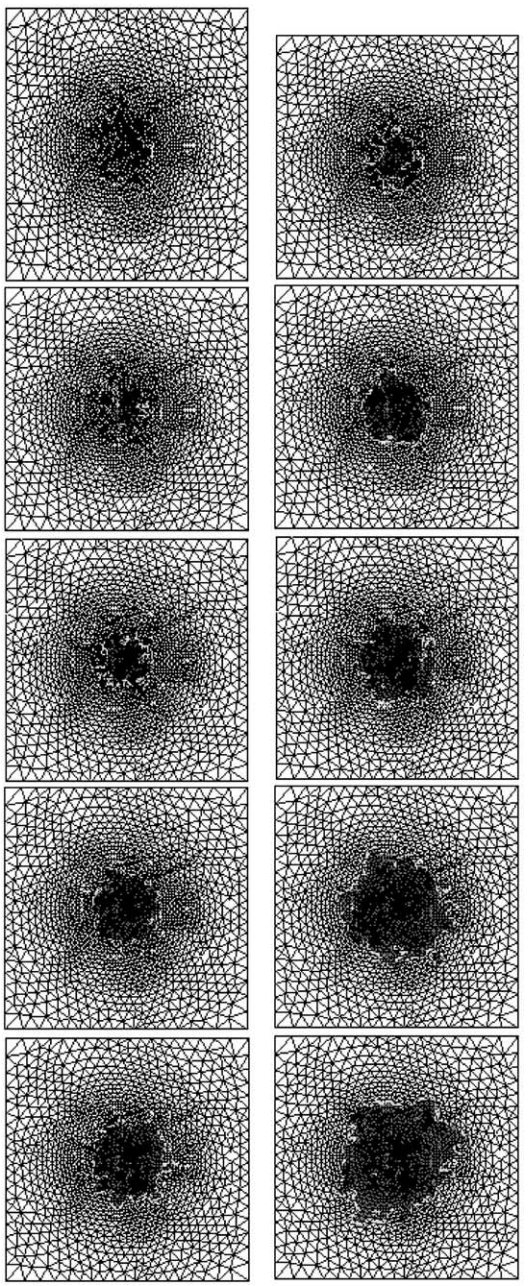

Fig. 10. Fracture patterns at different layers of the composite mesh (from top to bottom) at (a) $t =$ 0.0136s and (b) $t = 0.0245$s.

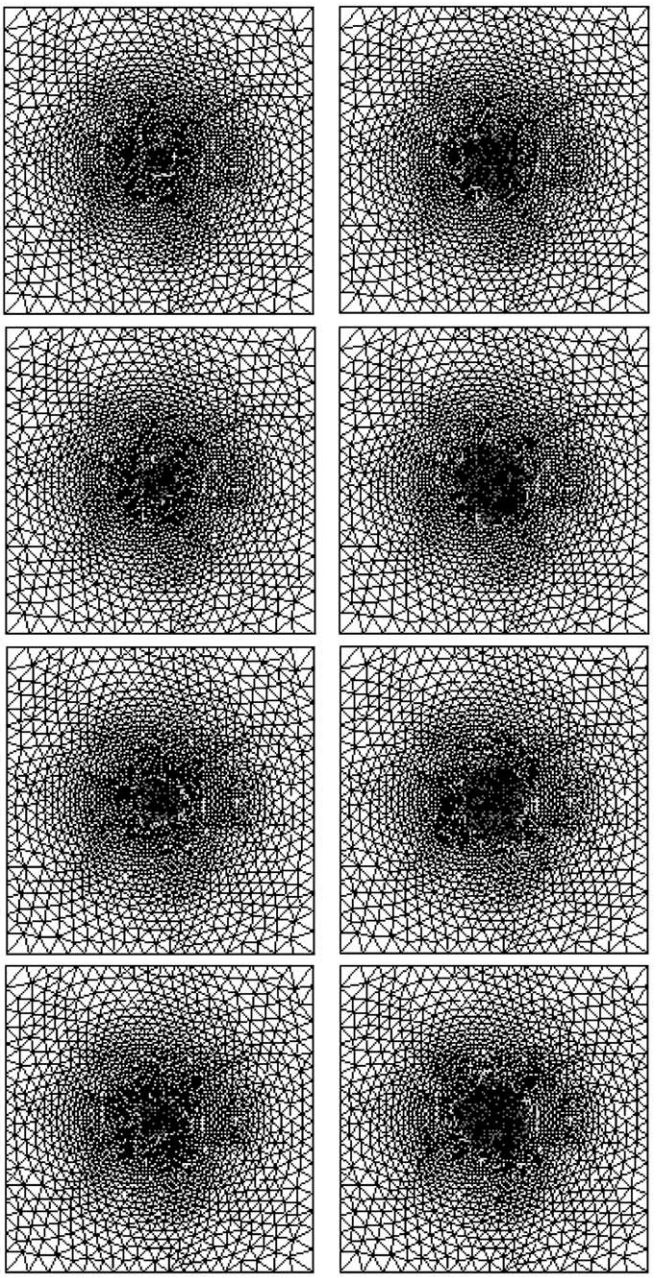

Fig. 11. Delamination patterns at the top to bottom interfaces of the composite mesh: at (a) $t =$ 0.0136s and (b) $t = 0.0245$s.

References

[1] Chen W-H, Yang Sh-H. Multilayer hybrid-stress finite element analysis of composite laminates with delamination cracks origination from transverse cracking. Eng Fract Mech 1996;54(5):713–29.
[2] Hashagen F, de Borst R. Numerical assessment of delamination in fibre metal laminates. Comput Methods Appl Mech Eng 2000;185:141–59.
[3] Hill R. A theory of yielding and plastic flow of anisotropic materials. Proc R Soc, A 1948;193:281–97.
[4] Hoffman O. The brittle strength of ortotropic materials. J Compos Mater 1967;1:200–6.
[5] Kwon YW, Aygunes H. Dynamic finite element analysis of laminated beams with delamination cracks using contact-impact conditions. Comput Struct 1996;58(6):1161–9.
[6] Liu S, Kutlu Z, Chang FK. Matrix cracking-induc delamination propagation in graphite/epoxy laminated composites due to a transverse concentrated load. In: Ashbangh NE, Stinchcomb WW, editors. Composite materials: fatigue and fracture. ASTM STP 1156, vol. 4. Philadelphia: ASTM; 1156. p. 86–101.
[7] Mi Y, Crisfield MA. Analytical derivation of load/displacement relationship for the DCB and MMB and proof of the FEA formulation. IC-AERO Report 97-02. Department of Aeronautics, Imperial College, London, UK; 1996.
[8] Mi Y, Crisfield MA, Davies GAO, Hellweg H-B. Progressive delamination using interface elements. J Compos Mater 1998;32(14):1246–72.
[9] Mohammadi S, Owen DRJ, Perić D. 3D progressive damage analysis of composites by combined finite/discrete element approach. In: European Congress on Computational Methods in Applied Science and Engineering ECCOMAS. 2000. [Barcelona, published on CD].
[10] Mohammadi S, Owen DRJ, Perić D. A combined finite/discrete element algorithm for delamination analysis of composites. Finite Elem Anal Des 1998;28:321–36.
[11] O'Brien. Analysis of local delaminations and their influence on composite laminate behaviour. In: Johnson WS, editor. Delamination and debonding of materials. ASTM STP 876. Philadelphia: ASTM; 1985. p. 282–97.
[12] Parker AP. The mechanics of fracture and fatigue, an introduction. E. & F.N. SPON Ltd.; 1981. p. 89–122.
[13] Rowlands RE. Strength (failure) theories and their experimental correlation. In: Sih GC, Skudra AM, editors. Handbook of composites, vol. 3—failure mechanics of composites. Amsterdam: Elsevier; 1985. p. 71–125 [chapter 2].
[14] Schellekens JCJ. Computational strategies for composite structures. PhD thesis. Technische Universiteit Delft, Holland; 1992.
[15] Sprenger W, Gruttmann F, Wagner W. Delamination growth analysis in laminated structures with continuum-based 3D-shell elements and a viscoplastic softening model. Comput Methods Appl Mech Eng 2000;185:123–39.
[16] Stravroulakis GE, Panagiotopoulos PD. On the interface debonding and frictional sliding in composites: the material inclusion problem. In: Johnson WS (editor). Delamination and debonding of materials; 1985. p. 165–72.
[17] Worswick MJ, Strazincky PV, Majeed O. Dynamic fracture of fibre reinforc composite coupons. In: Sun CT, Sankar BV, Rajapakse YDS, editors. Dynamic response and behaviour of composites. ASME AD, vol. 46. New York: ASME; 1995. p. 29–41.